Experimental and numerical modeling of a sloshing problem in a stepped based rectangular tank

Cite as: Phys. Fluids 33, 033111 (2021); https://doi.org/10.1063/5.0044682
Submitted: 18 January 2021 . Accepted: 04 March 2021 . Published Online: 24 March 2021

Tomás Gándara, Ernesto Castillo Del Barrio, Marcela Cruchaga, Joan Baiges, et al.

Physics of Fluids ARTICLE scitation.org/journal/phf

Experimental and numerical modeling of a sloshing problem in a stepped based rectangular tank

Cite as: Phys. Fluids 33, 033111 (2021); doi: 10.1063/5.0044682
Submitted: 18 January 2021 · Accepted: 4 March 2021 ·
Published Online: 24 March 2021

Tomás Gándara,[1,a] Ernesto Castillo Del Barrio,[1,b] Marcela Cruchaga,[1,c] and Joan Baiges[2,d]

AFFILIATIONS

[1]Universidad de Santiago de Chile, Avenida Libertador Bernardo O'Higgins 3363, Santiago, Chile
[2]Universitat Politècnica de Catalunya, Jordi Girona 1-3, Edifici C1, 08034, Barcelona, Spain

[a]Electronic mail: tomas.gandara@usach.cl
[b]Author to whom correspondence should be addressed: ernesto.castillode@usach.cl
[c]Electronic mail: marcela.cruchaga@usach.cl
[d]Electronic mail: joan.baiges@upc.edu

ABSTRACT

In this study, the two-dimensional sloshing of water in a stepped based tank partially filled was analyzed using an arbitrary Lagrangian–Eulerian adaptive fixed-mesh method and including the Smagorinsky turbulence model. The numerical model is verified by contrasting the predictions made by the model with experimental results. The tank was subjected to controlled one-directional motion imposed using a shake table. The free surface evolution was followed using ultrasonic sensors, and a high-speed camera was used to record the experiments. The experimental and numerical analyses include a comparison of the wave height at different control points and snapshots of the free surface evolution for two imposed frequencies. Also, a detailed numerical study of the effects of the frequency of the imposed movement, the step height, and the fluid volume on the wave dynamics was performed. Moreover, the effect of fluid viscosity on the dynamics of the free surface was also studied. In brief, the numerical method proved to be accurate, experimental data were reported, and the effects on the numerical results of different physical and numerical aspects were exhaustively analyzed. The proposed results help to understand the sloshing of stepped geometries.

I. INTRODUCTION

Analysis of tanks partially filled with liquid and subjected to external loads, which is known as sloshing, focuses on determining the behavior of the free surface and how internal hydrodynamic loads affect system stability.[1–5] Several researchers have attempted to develop analytical, experimental, and numerical methods for solving this type of problem.[6–9]

The sloshing response mainly depends on the excitation forces, the shape of the container, and the filling level. Evaluation of the vibration modes and natural frequencies is necessary for analyzing such problems. Thus, many studies have developed analytical solutions based on multi-modal non-linear potential theory, such as Ref. 10, where planar and non-planar behaviors are described for the lower natural frequencies. Moreover, experiments have been performed to validate the proposed analytical and numerical models. Sloshing in tanks with rectangular cross sections under controlled harmonic linear motion was studied in Refs. 11–14 for 2D and 3D behaviors. Analyses using tanks with other types of cross sections have also been performed.[15–19] Modified tank geometries have been proposed to evaluate the effect of baffles on wave height evolution and the associated dynamic forces on the container.[20–22] In this regard, a study on the effect of an abrupt change in the height of the tank will facilitate future comparisons of numerical methods.

The Navier–Stokes equations, including an appropriated description for the free surfaces and a discretized numerical method, are commonly applied to simulate sloshing problems. In this context, fixed- or moving-mesh strategies have been proposed. Fixed-mesh techniques solve the Navier–Stokes equations in the entire domain occupied by two fluids (e.g., air and water), and the interface between them has to be updated in a timely manner during analysis. To this end, the volume of fluid (VOF)[5,23–25] and level set (LS)[26,27] methods have been widely employed. Alternative techniques have also been proposed

(e.g., Refs. 28 and 29). Moving-mesh techniques are those in which the varying domain is adjusted at each time step using a new spatial discretization. These techniques can be used to solve a one-fluid flow problem. The arbitrary Lagrangian–Eulerian (ALE) technique[30,31] and the deforming spatial-domain/space-time (DSD/ST) technique[32,33] are effective methods to solve free-surface problems. A summary of numerical techniques applied to free surfaces and moving interfaces can be found in Ref. 34.

The mesh quality and refinement near the free surface are crucial aspects for obtaining an accurate description of the free surface.[35–38] These requirements for mesh quality and refinement are particularly difficult to fulfill when standard ALE techniques are applied for highly dynamic problems, because of the strong distortion of the meshes. The mesh in these cases can deform to a non-applicable configuration, and consistent remeshing techniques are required.[39–42] Therefore, mixed methods that combine fixed-mesh capabilities with ALE techniques have been developed more recently.[43] In this type of formulation, the fluid-dynamics equations are solved in a fixed based mesh for a two-fluid flow problem. The free surface is updated over such a mesh using ALE techniques. At each time step, after the updated interface is computed, the free surface is projected onto the base mesh, and local refinement of the base mesh is performed near the interface. This algorithm has been successfully applied to free surface evolution[44,45] and fluid-solid interaction problems.[46,47] In this framework, an adaptive mesh-refinement technique was developed.[48,49] In addition, a variational multiscale (VMS) principle was employed to build a weak form of the Navier–Stokes equations.[50] The resulting algorithm was used to analyze an oil-sloshing problem in a square cross section,[19] and the model was validated through experiments. The results demonstrated that the main natural frequencies are practically independent of fluid viscosity.

In this study, we present an exhaustive numerical analysis of an original sloshing experiment. The simulation is based on a free-surface strategy using a fixed-mesh ALE[19,48–50] approach. The fluid-dynamics equations were solved using a VMS finite-element technique previously evaluated on benchmark tests using Newtonian and non-Newtonian fluids.[51–53] The experiment was performed using a stepped based tank with a rectangular cross section having an aspect ratio of 1:8, which ensures planar wave behavior. The tank was mounted on a shake table and was subjected to controlled one-dimensional motion. The free-surface evolution was recorded using ultrasonic sensors and a high-speed camera to ensure accurate experimental observations. Owing to the tank geometry, the obtained wave pattern strongly varied with the time and position. Therefore, the simulation of this experiment was challenging. In this work, experimental data were compared with the numerical predictions to validate the model. Moreover, the effects of parameters such as the mesh size, refinement during remeshing, time step size, time-integration schemes, turbulence effects, filling level, step height, and fluid type on the numerical results were evaluated.

The main contributions of this work are as follows:

- A sloshing experiment on stepped based tanks was conducted.
- The proposed numerical model was validated using experimental data.
- The effect of different physical and numerical parameters on the numerical results was exhaustively analyzed.
- The evaluated numerical aspects assist in understanding the physical aspects of the sloshing of stepped geometries.

The remainder of this paper is organized as follows: The governing equations and the adopted numerical strategy are described in Sec. II. The experimental settings and the details of the experiment are presented in Sec. III. The model validation and numerical assessment of different modeling aspects are reported in Sec. IV. Finally, the conclusions are presented in Sec. V.

II. PROBLEM STATEMENT AND FINITE ELEMENT DISCRETIZATION

A. Boundary value problem

The equations of conservation of momentum and mass in the differential form for incompressible fluids may be expressed for a fixed domain as follows:

$$\rho\frac{\partial \boldsymbol{u}}{\partial t}+\rho\boldsymbol{u}\cdot\nabla\boldsymbol{u}-\nabla\cdot(2\eta\nabla^{s}\boldsymbol{u})+\nabla p=f,\quad \text{in}\,\Omega,t\in]0,t_f[, \tag{1}$$

$$\nabla\cdot\boldsymbol{u}=0\,,\quad \text{in}\,\Omega,t\in]0,t_f[, \tag{2}$$

where Ω represents the computational domain with boundaries $\partial\Omega$ occupied by the fluid, $t\in]0,t_f[$ is the time interval in which the problem is solved, ρ and η denote the density and apparent viscosity of the fluid, respectively, $p:]0,t_f[\rightarrow\mathbb{R}$ is the pressure field, and $\boldsymbol{u}:]0,t_f[\rightarrow\mathbb{R}^d$ is the velocity vector, in which $d=2,3$ is the number of spatial dimensions. Regarding the right-hand side of Eq. (1), $\boldsymbol{f}=\rho\boldsymbol{g}^*$ represents a body force term that involves gravity and the acceleration of the fluid domain. The total acceleration is represented by $\boldsymbol{g}^*$. $\nabla^s\boldsymbol{u}$ represents the symmetrical gradient of the velocity $(\nabla^s\boldsymbol{u}=\frac{1}{2}(\nabla\boldsymbol{u}+(\nabla\boldsymbol{u})^T))$. These equations need to be solved simultaneously with appropriate initial and boundary conditions. For the Newtonian case, the apparent viscosity corresponds to the dynamic viscosity μ.

With regard to the rheological behavior of the fluid, the power-law constitutive model is used, which is defined as

$$\eta=m\dot{\gamma}^{n-1}, \tag{3}$$

where $\dot{\gamma}=\sqrt{\frac{1}{2}(\dot{\boldsymbol{\gamma}}:\dot{\boldsymbol{\gamma}})}$ represents the magnitude of the rate of the deformation tensor $\dot{\boldsymbol{\gamma}}=\nabla\boldsymbol{u}+(\nabla\boldsymbol{u})^T$, m represents the consistency index, and n is the power-law index of the fluid. If $n>1$, the fluid is called shear thickening or dilatant, and if $n<1$, the fluid is called shear thinning or pseudoplastic.

B. Fixed-mesh ALE formulation

In free-surface problems, the full domain represented by Ω can be split into two parts: the part of the domain effectively occupied by the fluid, $\Omega_1(t)$, and the remaining part, $\Omega\backslash\Omega_1(t)$. The moving boundary of $\Omega_1(t)$ is known as the free surface, and it can be represented as $\Gamma_{\text{free}}(t)$. Note that both $\Omega_1(t)$ and $\Gamma_{\text{free}}(t)$ are time-dependent and can change in time. The movement of the domain can be represented using an ALE domain velocity $\boldsymbol{u}_\Omega(\boldsymbol{x},t)\in\mathbb{R}^d$, where $\boldsymbol{x}\in\Omega$ are the spatial coordinates. We can define the bijective mapping $\boldsymbol{\lambda}$, so that for every point $\boldsymbol{X}\in\Omega$ and time instant t, we obtain a point $\boldsymbol{x}=\boldsymbol{\lambda}(\boldsymbol{X},t)$. With this definition, the domain velocity can be defined as

$$\boldsymbol{u}_\Omega(\boldsymbol{x},t)=\frac{\partial \boldsymbol{\lambda}(\boldsymbol{X},t)}{\partial t}. \tag{4}$$

For an ALE approach, the domain velocity generally does not coincide with the fluid velocity $\boldsymbol{u}$ in $\Omega_1(t)$. The effective conditions between domain velocity and velocity are defined by

$$\boldsymbol{n}\cdot\boldsymbol{u}_\Omega=\boldsymbol{n}\cdot\boldsymbol{u}\quad \text{in}\ \Gamma_{\text{free}}\cup\partial\Omega,$$

where $\boldsymbol{n}$ represents the outward normal of the point. With these definitions, the incompressible Navier–Stokes problem in the ALE frame of reference can be written as follows:

$$\rho\left.\frac{\partial \boldsymbol{u}}{\partial t}\right|_{\lambda}+\rho(\boldsymbol{u}-\boldsymbol{u}_\Omega)\cdot\nabla\boldsymbol{u}-\nabla\cdot(2\eta\nabla^s\boldsymbol{u})+\nabla p=f,\quad \text{in}\Omega,t\in]0,t_f[, \tag{5}$$

$$\nabla\cdot\boldsymbol{u}=0,\qquad \text{in}\,\Omega,t\in]0,t_f[. \tag{6}$$

More details regarding ALE methods can be found in Refs. 30, 43, and 54. A specific feature of the method used in this work is that after each time step, the results are projected from the deformed mesh to the initially underformed mesh, from which the simulation is continued. Thus, this method is a part of the fixed-mesh method family.

C. Variational and Galerkin form

We consider the finite element approximation of Eqs. (1) and (2). We define $\boldsymbol{\mathcal{V}}=(H^1(\Omega))^d$ and $\mathcal{Q}=L^2(\Omega)/\mathbb{R}$, which are the interpolation spaces of velocity and pressure, respectively, where $H^1(\Omega)$ is the space of functions whose distributional derivatives of order equal to one belong to $L^2(\Omega)$ vanishing on $\partial\Omega$. If we assume that $\boldsymbol{\mathcal{X}}:=\boldsymbol{\mathcal{V}}\times\mathcal{Q}$, the weak form of the problem is $\boldsymbol{U}=[\boldsymbol{u},p]:]0,t_f[\to\boldsymbol{\mathcal{X}}$ such that the initial conditions are satisfied and

$$\rho\left(\left.\frac{\partial \boldsymbol{u}}{\partial t}\right|_{\lambda},\boldsymbol{v}\right)+\langle\rho\boldsymbol{a}\cdot\nabla\boldsymbol{u},\boldsymbol{v}\rangle+2\eta(\nabla^s\boldsymbol{u},\nabla^s\boldsymbol{v})-(p,\nabla\cdot\boldsymbol{v})=\langle\boldsymbol{f},\boldsymbol{v}\rangle, \tag{7}$$

$$(\nabla\cdot\boldsymbol{u},q)=0, \tag{8}$$

for all $\boldsymbol{V}=[\boldsymbol{v},q]\in\boldsymbol{\mathcal{X}}$, where $\boldsymbol{f}$ is such that $\langle\boldsymbol{f},\boldsymbol{v}\rangle$ is well-defined and $\boldsymbol{a}=\boldsymbol{u}-\boldsymbol{u}_\Omega$ is the advective velocity. Here, $(\cdot,\cdot)$ denotes the $L^2(\Omega)$ inner product, and $\langle\cdot,\cdot\rangle$ represents the integral of the product of two functions, not necessarily in $L^2(\Omega)$.

In a compact form, problems (7) and (8) can be written as

$$\rho\left(\left.\frac{\partial \boldsymbol{u}}{\partial t}\right|_{\lambda},\boldsymbol{v}\right)+B(\boldsymbol{a};\boldsymbol{U},\boldsymbol{V})=\langle\boldsymbol{f},\boldsymbol{v}\rangle, \tag{9}$$

where

$$B(\boldsymbol{a};\boldsymbol{U},\boldsymbol{V})=(2\eta\nabla^s\boldsymbol{u},\nabla^s\boldsymbol{v})+\langle\rho\boldsymbol{a}\cdot\nabla\boldsymbol{u},\boldsymbol{v}\rangle-(p,\nabla\cdot\boldsymbol{v})+(\nabla\cdot\boldsymbol{u},q).$$

The Galerkin approximation for the variational problem can be performed by considering a finite element partition $\mathcal{T}_h$ of the domain Ω and the conforming finite element spaces, $\boldsymbol{\mathcal{V}}_h\subset\boldsymbol{\mathcal{V}}$ and $\mathcal{Q}_h\subset\mathcal{Q}$, in a usual manner.

To discretize in time, we use the first, second, and third orders in the time backward difference formula (BDF). This method allows us to define the following time-derivative expressions:

$$\frac{\partial \boldsymbol{u}_h^{j+1}}{\partial t}=\frac{\boldsymbol{u}_h^{j+1}-\boldsymbol{u}_h^{j}}{\delta t}+\mathcal{O}(\delta t), \tag{10}$$

$$\frac{\partial \boldsymbol{u}_h^{j+1}}{\partial t}=\frac{3\boldsymbol{u}_h^{j+1}-4\boldsymbol{u}_h^{j}+\boldsymbol{u}_h^{j-1}}{2\delta t}+\mathcal{O}(\delta t^2), \tag{11}$$

$$\frac{\partial \boldsymbol{u}_h^{j+1}}{\partial t}=\frac{11\boldsymbol{u}_h^{j+1}-18\boldsymbol{u}_h^{j}+9\boldsymbol{u}_h^{j-1}-2\boldsymbol{u}_h^{j-2}}{6\delta t}+\mathcal{O}(\delta t^3), \tag{12}$$

where δt represents the size of a uniform partition of the time interval $[0,t_f]$ and $\mathcal{O}(\cdot)$ represents the approximation order of the scheme. The superscript indicates the time step in which the variable is being approximated; thus, $\boldsymbol{u}^j$ is an approximation to $\boldsymbol{u}$ at time $t^j=j\delta t$. For brevity, we refer to the first-, second-, and third-order methods as BDF1, BDF2, and BDF3, respectively.

Smagorinsky's turbulence model was employed for the numerical simulations. This is a standard method for numerical modeling of water–air sloshing analyses.[34] The turbulent dynamic viscosity associated with this model is as follows:

$$\eta_{turb}=C_S h_1^2\left(\nabla^S\boldsymbol{u}_h:\nabla^S\boldsymbol{u}_h\right)^{\frac{1}{2}}, \tag{13}$$

where C_S is an algorithmic constant of the model (the Smagorinsky coefficient) and h_1 corresponds to a characteristic element length calculated as the square root of the element area in a two-dimensional case and the cubic root of the element volume in 3D. To simplify the nomenclature in the exposition of the method, the turbulent viscosity is included in the apparent viscosity of the fluid ($\eta=\eta+\eta_{turb}$).

D. Stabilized formulation

To use equal order interpolation and to solve convective-dominant cases, a stabilized formulation is needed. The stabilized method used in this study is based on the VMS approach introduced in Ref. 55. A detailed derivation of the method used can be found in Ref. 56 for the Navier–Stokes problem. Herein, we simply state the method for the problem defined by (7) and (8). After some approximations, this method involves finding $\boldsymbol{U}_h:]0,t_f[\to\boldsymbol{\mathcal{X}}_h$ such that

$$\rho\left(\frac{\partial \boldsymbol{u}_h}{\partial t},\boldsymbol{v}_h\right)+B(\boldsymbol{a}_h;\boldsymbol{U}_h,\boldsymbol{V}_h)+S_1(\boldsymbol{a}_h;\boldsymbol{U}_h,\boldsymbol{V}_h)+S_2(\boldsymbol{U}_h,\boldsymbol{V}_h)=\langle\boldsymbol{f},\boldsymbol{v}_h\rangle, \tag{14}$$

for all $\boldsymbol{V}_h\in\boldsymbol{\mathcal{X}}_h$, where

$$\begin{aligned}S_1(\boldsymbol{a}_h;\boldsymbol{U}_h,\boldsymbol{V}_h)=\sum_K\alpha_1\langle\boldsymbol{f}-\rho\frac{\partial \boldsymbol{u}_h}{\partial t}-\rho\boldsymbol{a}_h\cdot\nabla u_h+\eta\Delta\boldsymbol{u}_h-\nabla p_h,\\ -\rho\boldsymbol{a}_h\cdot\nabla\boldsymbol{v}_h-\eta\Delta\boldsymbol{v}_h-\nabla q_h\rangle_K,\\ S_2(\boldsymbol{U}_h,\boldsymbol{V}_h)=\sum_K\alpha_2\langle\nabla\cdot\boldsymbol{u}_h,\nabla\cdot\boldsymbol{v}_h\rangle_K.\end{aligned}$$

In the above equations, $\boldsymbol{\alpha}$ represents a matrix computed within each element, called the matrix of stabilization parameters, which provides dimensional consistency to the stabilized terms. These parameters are defined as follows:

$$\boldsymbol{\alpha}=\text{diag}(\alpha_1\boldsymbol{I}_d,\alpha_2), \tag{15}$$

with $\boldsymbol{I}_d$ being the identity on vectors of $\mathbb{R}^d$. The parameter α_i, with $i=1,2$, can be computed as follows:

$$\alpha_1 = \left[c_1 \frac{\eta}{h_1^2} + c_2 \frac{\rho |\boldsymbol{a}_h|}{h_2} \right]^{-1}, \quad \alpha_2 = \frac{h_1^2}{c_3 \alpha_1}. \tag{16}$$

In these expressions, h_1 corresponds to a characteristic element length calculated in the same manner as in the Smagorinsky case, and h_2 corresponds to another characteristic length calculated as the element length in the streamline direction. The constants c_i, $i = 1, \ldots, 3$, are algorithmic parameters in the formulation. The values used in this work are $c_1 = 12$, $c_2 = 2$, and $c_3 = 4$, which can be derived from numerical analysis of the one-dimensional convection-diffusion-reaction problem.[57] These values have been proven to be robust for different problems, including those involving Newtonian and non-Newtonian fluids and for different applications.[52,53,58]

The aforementioned stabilized formulation ensures global stability. To overcome the local instabilities caused by the cut elements, a method known as ghost penalty stabilization is employed. This method ensures control of a given field in the cut elements without affecting the convergence rate of the numerical formulation.[59] In summary, the terms added to (14) are

$$S_{ghost}(\boldsymbol{a}_h; \boldsymbol{U}_h, \boldsymbol{V}_h) = \sum_K \left(c_4 h_1^2 \alpha_1^{-1} \right) \langle \nabla \boldsymbol{v}_h, P_{\boldsymbol{u}}^{\perp}(\nabla \boldsymbol{u}_h) \rangle_{K(\Omega_{cut}(t))} + \sum_K (c_5 \alpha_2) \langle \nabla q_h, P_p^{\perp}(\nabla p_h - \boldsymbol{f}) \rangle_{K(\Omega_{cut}(t))}, \tag{17}$$

where $\Omega_{cut}(t)$ represents the domain of the K element cut by the free surface $\Gamma_{\text{free}}(t)$; c_4 and c_5 are algorithmic constants, both assumed to be 0.1 in this study; and $P^{\perp}$ represents the orthogonal projections in the cut elements, which are defined as follows:

$$P_{\boldsymbol{u}}^{\perp}(\nabla \boldsymbol{u}_h) = \nabla \boldsymbol{u}_h - P_{\boldsymbol{u}}(\nabla \boldsymbol{u}_h),$$
$$P_p^{\perp}(\nabla p_h - \boldsymbol{f}) = (\nabla p_h - \boldsymbol{f}) - P_p(\nabla p_h - \boldsymbol{f}),$$

where $P_{\boldsymbol{u}}$ represents the $L^2(\Omega)$ projection onto $\boldsymbol{\mathcal{V}}_h$ and P_p the $L^2(\Omega)$ projection onto $\mathcal{Q}_h$.

E. Tracking of the interface

For tracking the interface, the LS method is employed, which is based on the pure advection of a smooth function, commonly defined as $\phi(\boldsymbol{x}, t)$, over the entire domain Ω. This function allows for defining the position of the front of the interface using the isovalue $\phi(\boldsymbol{x}, t) = \phi_c$.

The conservation of ϕ in any control volume $V_t \subset \Omega$ moving with a divergence-free velocity field $\boldsymbol{u}$ can be defined in an ALE frame using the following equation:

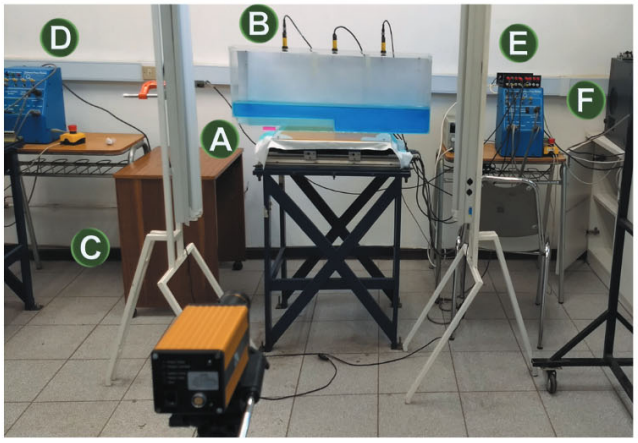

FIG. 1. Experimental setup. Tank mounted on the shake table (A), ultrasonic sensors (B), high-speed camera (C), shake table controller [(D) and (E)], and PC (F).

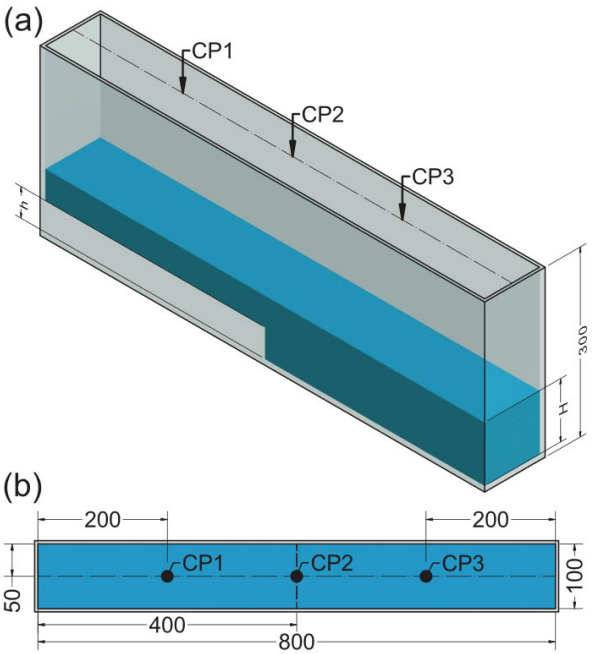

FIG. 2. Layout of the tank used with (a) elevation and (b) isometric views with internal dimensions in mm.

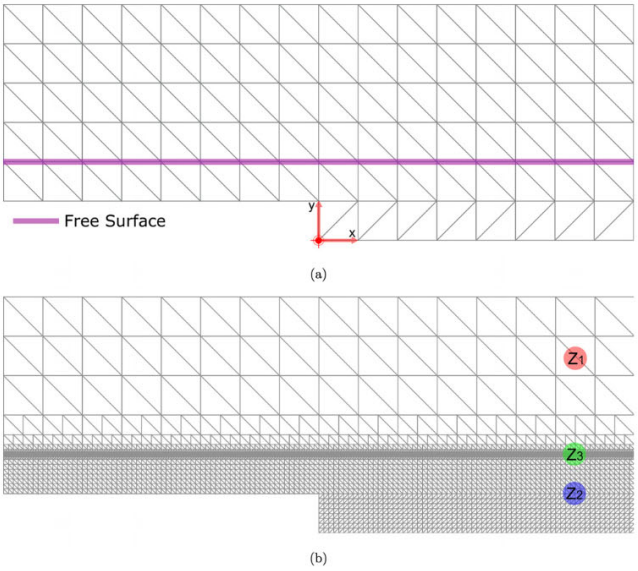

FIG. 3. Finite element mesh employed: (a) initial mesh (without adaptivity) and (b) with adaptive refinement (see the element sizes in Table I).

TABLE I. Nodes, elements, and elementary lengths (Δx and Δy) in mm of the elements in zones Z_1, Z_2, and Z_3 in an adapted mesh.

Mesh	Nodes	Elements	Z_1		Z_2		Z_3	
			Δx	Δy	Δx	Δy	Δx	Δy
M_1	5835	10 592	100	83.33	12.5	10.416 3	1.562 5	1.302
M_2	11 440	20 768	50	50	6.25	6.25	0.782 5	0.782 5
M_3	16 567	30 480	40	31.25	5	3.906 2	0.625	0.488

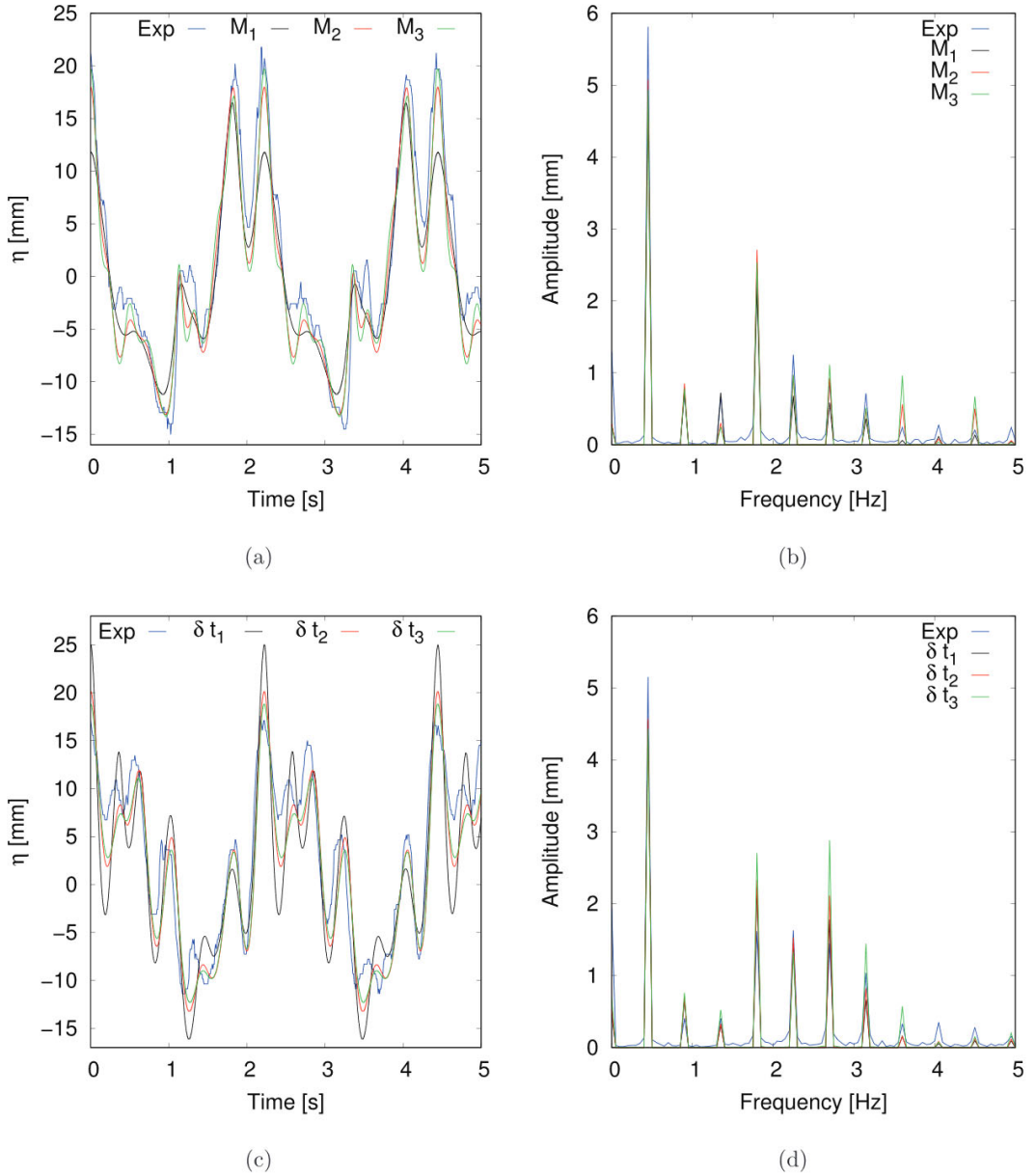

FIG. 4. Comparison between experimental and numerical data for $f = 0.45$ Hz. [(a) and (b)] mesh (M_i) convergence at CP1 and [(c) and (d)] time step (δt_i) convergence in CP3 of the free surface time-dependent behavior (left) and its FFT (right).

TABLE II. Five principal active frequencies in order of amplitude, obtained using the FFT of experimental and numerical responses at CP1. f_k is in Hz, and A_k is in mm.

	Experimental		M_1—δt_2		M_2—δt_2		M_3—δt_2		M_2—δt_1		M_2—δt_3	
	f_k	A_k	f_k	A_k	f_k	A_k	f_k	A_k	f_k	A_k	f_k	A_k
f_1	0.45	5.81	0.45	4.62	0.45	5.08	0.45	4.94	0.45	4.81	0.45	5.03
f_2	1.8	2.44	1.8	2.18	1.8	2.71	1.8	2.54	1.8	2.55	1.8	2.6
f_3	2.25	1.25	0.9	0.73	2.25	0.97	2.7	1.11	2.7	1.2	2.25	0.9
f_4	2.7	0.87	1.35	0.72	2.7	0.93	2.25	0.97	2.25	0.91	0.9	0.83
f_5	0.9	0.75	2.25	0.68	0.9	0.85	3.6	0.96	0.9	0.8	2.7	0.83

$$\frac{\partial \phi}{\partial t} + \boldsymbol{a} \cdot \nabla \phi = 0, \quad \text{in}\,\Omega, t \in]0, t_f[, \tag{18}$$

with the corresponding initial and boundary conditions. The advection velocity is defined as $\boldsymbol{a} = \boldsymbol{u} - \boldsymbol{u}_\Omega$.

In this study, the level set equation (18) was solved using the classical streamline upwind Petrov–Galerkin method[60] to stabilize the convective nature of the equation. The time derivative was discretized in the same manner as the velocity in the momentum equation. Additionally, to integrate the physical properties appropriately in the computational domain, a modified integration rule was used in the elements cut by the interface.[49]

The advection of the LS function does not guarantee global mass conservation. In the present work, we used a very simple method to ensure global mass conservation. The method involves measuring the total mass at the end of each time step and computing the amount of mass lost; then, the LS function is displaced accordingly in a uniform global manner in the direction orthogonal to the free surface to recover the lost mass (see Ref. 49 for more details).

F. Adaptive-mesh approach

A key aspect of the numerical simulations presented herein is an adaptive mesh-refinement strategy that tracks the position of the free surface and allows us to obtain accurate solutions using a reasonably small number of elements. For this purpose, the fixed-mesh ALE method is coupled with the parallel adaptive mesh-refinement library RefficientLib.[48] When adaptive refinement approaches are used for free-surface problems, in many cases, the precision of the numerical simulation depends primarily on the accuracy with which the interface between the two materials is tracked.[19] Thus, an adaptive mesh-refinement criterion based on layers of elements around the fluid interface is used. An important characteristic of the method is that it enables the use of non-conforming elements, thus optimizing the transitions between large and small elements.[49]

III. EXPERIMENTAL WORK

A stepped based tank with a rectangular cross section having an aspect ratio of 1 : 8 and a step height of $h = 50$ mm, fabricated using acrylic, was filled with water up to a height of $H = 100$ mm and mounted on the shake table (see Figs. 1 and 2). The shake table is driven by an engine that produces a screw-controlled, time-varying motion with micrometers of precision and up to 2.5 g accelerations, depending on the weight loaded [see Quanser (2013) STII Manual in http://www.quanser.com]. A controlled sinusoidal motion with an amplitude of $A = 7.5$ mm and frequencies $f = 0.45$ Hz and $f = 0.5$ Hz was imposed on the tank. The free-surface evolution $\eta(t)$ mm was recorded using ultrasonic sensors located at three control points (CP1, CP2, and CP3), as shown in Fig. 2. The positions of the sensors were chosen to avoid interference between the tank walls and the ultrasonic signal. In addition, the step-control points were located at strategic positions: the first one (CP1) was at the center of the shallow region, the second (CP2) was immediately above the step, and the third one (CP3) was in the middle of the deepest zone.

The sensors used in this work are the BANNER ultrasonic sensor model S18UUA with analog output (see the U-GAGE S18U series datasheet in www.bannerengineering.com). Its operating principle is based on sending a pulse of 300 kHz to a surface, reporting an output voltage between 0 V and 10 V, corresponding to a position range between 30 mm and 300 mm with an accuracy of $\pm 0, 5$ mm for a time response of 5 ms. The experiments were also recorded using a high-speed camera at a resolution of 1969×800 px^2 and 120 fps. The field of view covers the tank size geometry depicted in Fig. 2 and its imposed displacement, i.e., 810×300 mm^2 approximately. The camera is positioned in a fixed location from the tank, and a lens of 35 mm

TABLE III. Five principal active frequencies in order of amplitude, obtained using the FFT of experimental and numerical responses at CP3. f_k is in Hz, and A_k is in mm.

	Experimental		M_1—δt_2		M_2—δt_2		M_3—δt_2		M_2—δt_1		M_2—δt_3	
	f_k	A_k	f_k	A_k	f_k	A_k	f_k	A_k	f_k	A_k	f_k	A_k
f_1	0.45	5.15	0.45	4.23	0.45	4.57	0.45	4.45	0.45	4.43	0.45	4.55
f_2	1.8	1.62	1.8	1.91	1.8	2.33	2.7	2.52	2.7	2.88	1.8	2.23
f_3	2.25	1.63	2.25	1.07	2.7	2.11	1.8	2.35	1.8	2.72	2.7	1.78
f_4	2.7	1.45	2.7	0.99	2.25	1.53	2.25	1.32	2.25	1.33	2.25	1.44
f_5	3.15	1.04	0.9	0.58	3.15	0.83	3.15	1.09	3.15	1.45	0.9	0.67

is used; this lay-out was also tested in Refs. 19, 22, and 61. The measurements are previously verified by contrasting rules and objects used as patterns to avoid optical errors. The camera is aligned considering the water level at rest. The free-surface position obtained from the ultrasonic sensors was confirmed against the position obtained from the post-processed video using a motion-capturing technique previously used in Ref. 19. Alternatives and additional explanation on motion capturing techniques can be found in Refs. 22 and 61. As ultrasonic records can be affected by highly distorted free-surface patterns, this check helps to confirm that the free-surface distortion is within the required range to produce correct ultrasonic records. These experimental procedures and laboratory facilities were also used in Refs. 11, 13, 14, and 19. Observations along the thickness of the tank are made to confirm differences in the water level along it, i.e., to determine the occurrence of 3D effects. No differences between the water level in the front and back of the tank were found at least within the error bound. Sloshing at the frequency of $f = 0.45$ Hz was considered as a reference case in this study. The experimental results are presented in Sec. IV, together with the numerical results.

IV. NUMERICAL RESULTS

In this study, a numerical analysis was performed using the fixed-mesh ALE finite element formulation presented in Sec. II D. In this section, we verify the accuracy of the method for modeling an experimental set of results for sloshing of a planar-step geometry partially filled with water. The experiment was performed specifically for

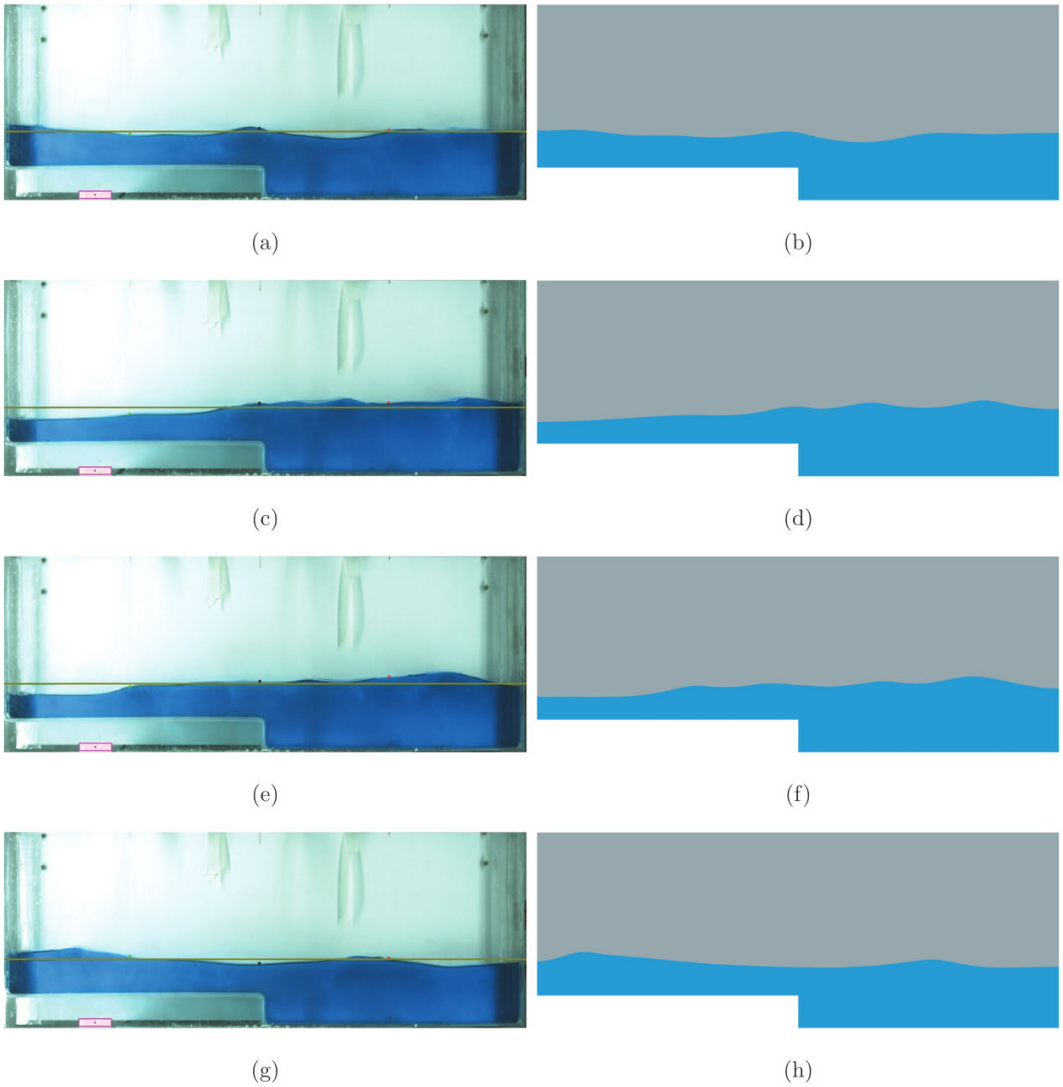

FIG. 5. Experimental (left) and numerical (right) snapshots of the free-surface evolution. [(a) and (b)] $3/8T$, [(c) and (d)] $3/5T$, [(e) and (f)] $3/4T$, and [(g) and (h)] T, with $f = 0.45$ Hz (T period, $T = 1/f$ s).

this study. Additionally, this section presents a sensitivity study of some parameters of the mathematical model used, including spatial and temporal discretization and the effect of the Smagorinsky coefficient on the numerical approximation (Subsection IV B). The effects of the imposed frequency and the step height of the tank are also described in Secs. IV C and IV D. Finally, a study of the effect of viscosity on wave dynamics is included for Newtonian and non-Newtonian fluids in Sec. IV E.

A. Numerical validation

In this subsection, the experimental results of the case with $f = 0.45$ Hz defined in Sec. III are numerically obtained and compared. Because the experiment presents well-defined plane (2D) behavior, the simulations were performed using a bidimensional geometry. The fluid properties used for water were $\rho = 998.2$ kg/m^3 and $\mu = 0.001$ Pa s.

The first set of results is related to a mesh-convergence analysis. Three non-conforming meshes (M_i, $i = 1, \ldots, 3$) with different element sizes were used. Because adaptive meshes were used, Fig. 3(a) shows the details of the original mesh (without adaptivity) and Fig. 3(b) shows an arbitrarily adapted mesh. This figure depicts the M_2 mesh. The details of each mesh are provided in Table I. Note that the meshes have different element sizes depending on their locations. We can distinguish three zones, denoted as Z_i, $i = 1, \ldots, 3$. Zone 1 (Z_1) represents the region occupied by air from the physical viewpoint. Because the problem is solved without considering air–water interaction, it can be discretized with large elements. Zone 2 (Z_2) corresponds to the fluid region (water in the base case) that is far from the interface.

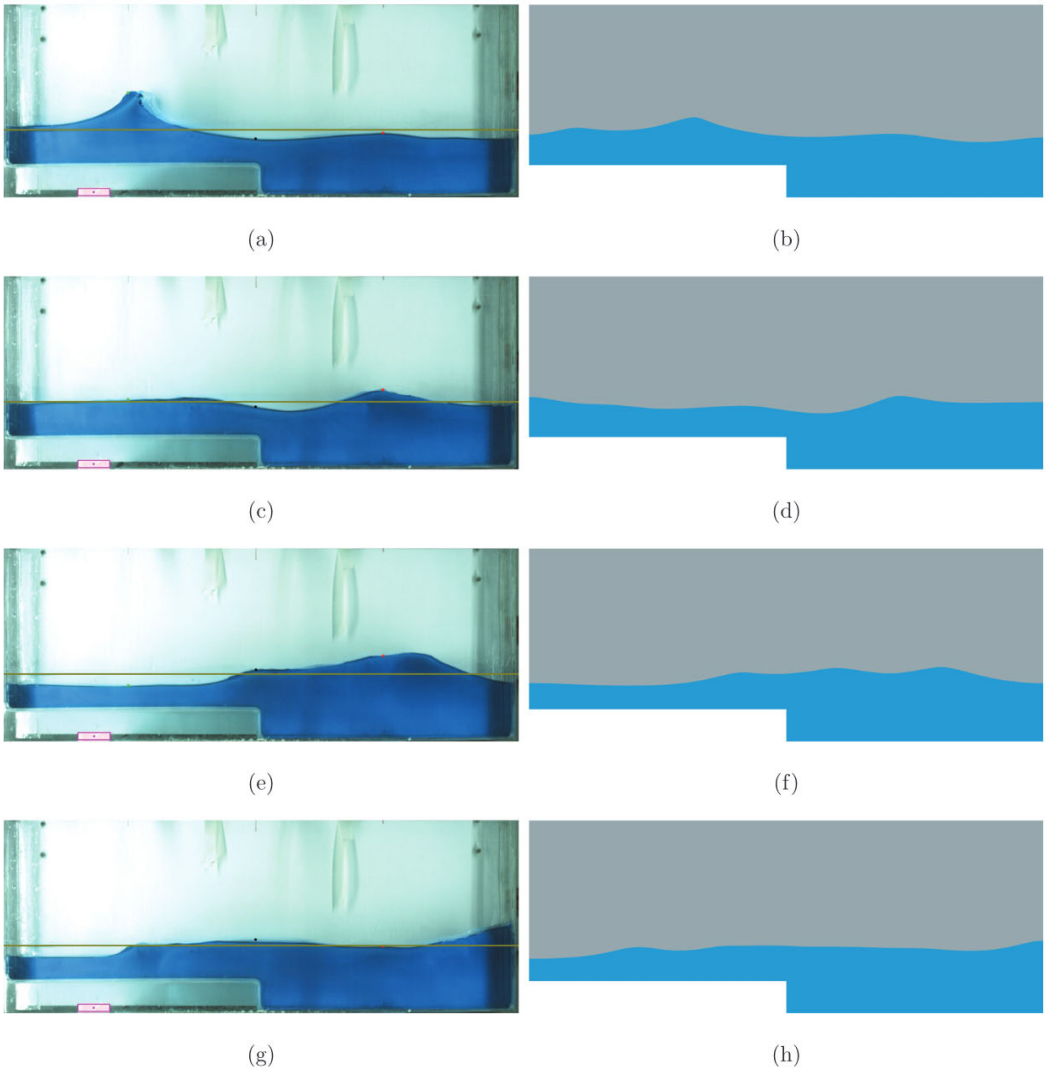

FIG. 6. Experimental (left) and numerical (right) snapshots of the free-surface evolution. [(a) and (b)] $1/4T$, [(c) and (d)] $1/2T$, [(e) and (f)] $3/4T$, and [(g) and (h)] $9/10T$, with $f = 0.5$ Hz.

Finally, Zone 3 (Z_3) represents the region of space that contains the interface and, therefore, must have the smallest discretization. Note that the use of non-conforming meshes allows for large transitions between large and small elements without increasing the number of total elements.

Table I shows that the number of nodes and elements is small because of the adaptivity and considering the small size of the elements over the interface. For example, using a structured and isotropic mesh with the size of its elements equal to zone Z_3 of the M_2 mesh, the number of nodes and elements needed is 360 128 and 717 444, respectively.

To study the convergence in time, three time step values were used: $\delta t_1 = 0.002$ s, $\delta t_2 = 0.001$ s, and $\delta t_3 = 0.000\,5$ s. To ensure that the convergence in time analysis is independent with the spatial/temporal discretization, the second order in the time scheme and a Smagorinsky coefficient $C_S = 0.1$ were used. The effect of the wave dynamics of these two numerical parameters is discussed in Sec. IV B.

In Fig. 4, the results obtained with the three meshes [Fig. 4 (top)] and the three time steps [Fig. 4 (bottom)] mentioned above are compared. For mesh convergence, a fixed value of $\delta t = \delta t_2 = 0.001$ s was used, whereas for time convergence, mesh M_2 was used. The

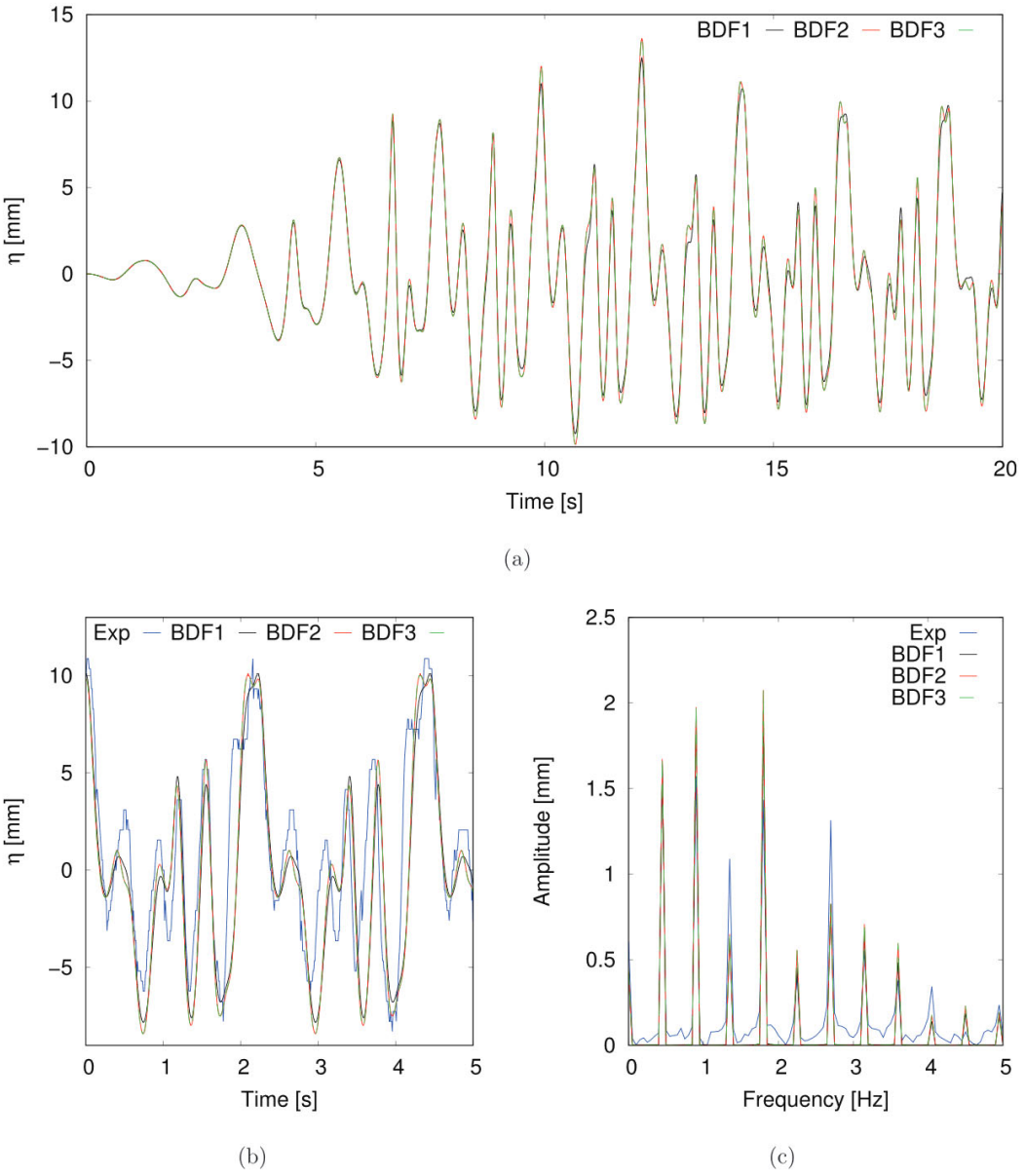

FIG. 7. Influence of the time integrator scheme (BDF) on wave evolution at CP2 for (a) the initial transient and [(b) and (c)] steady-state flow regimes; case with $f = 0.45$ Hz (left) and its FFT (right).

TABLE IV. Five principal active frequencies in order of amplitude obtained using FFT of experimental and numerical time integration scheme responses at CP2. f_k is in Hz, and A_k is in mm.

	Experimental		BDF1		BDF2		BDF3	
	f_k	A_k	f_k	A_k	f_k	A_k	f_k	A_k
f_1	0.45	1.6	0.9	1.94	1.8	2.08	1.8	2.07
f_2	0.9	1.57	1.8	1.9	0.9	1.98	0.9	1.98
f_3	1.8	1.43	0.45	1.64	0.45	1.67	0.45	1.67
f_4	2.7	1.32	2.7	0.82	2.7	0.83	2.7	0.83
f_5	1.35	1.09	3.15	0.66	3.15	0.71	3.15	0.71

TABLE V. Five principal active frequencies in order of amplitude obtained using FFT of experimental and numerical Smagorinsky-coefficient responses at CP3. f_k is in Hz, and A_k is in mm.

	Experimental		C_S 0.05		C_S 0.10		C_S 0.15		C_S 0.20	
	f_k	A_k	f_k	A_k	f_k	A_k	f_k	A_k	f_k	A_k
f_1	0.45	5.15	0.45	4.57	0.45	4.57	0.45	4.56	0.45	4.54
f_2	2.25	1.63	1.8	2.36	1.8	2.33	1.8	2.3	1.8	2.29
f_3	1.8	1.62	2.7	2.2	2.7	2.11	2.7	2.04	2.7	1.97
f_4	2.7	1.45	2.25	1.49	2.25	1.53	2.25	1.53	2.25	1.52
f_5	3.15	1.04	3.15	0.84	3.15	0.83	3.15	0.81	3.15	0.78

results are related to the evolution of the height of the free surface at CP1 and CP3 for the fully developed in time flow behavior, in addition to the respective fast Fourier transform (FFT) diagrams. In the evolution graph, positive values ($\eta > 0$ mm) correspond to heights over the fluid height in the rest state, whereas negative values ($\eta < 0$ mm) represent heights below the aforementioned reference value. The figure includes the experimental and numerical results.

Figure 4 confirms that the spatial and temporal discretizations used are sufficiently fine to represent wave dynamics. The mesh with the best correlation with the experimental results was M_2. For the time step, δt_2 resulted in a better fit of the height-evolution curve with the experimental results than δt_1 does; the smallest time step, δt_3, was discarded because it did not present significant improvements with respect to δt_2. The differences between M_1, M_2, and M_3 were small, and thus, M_2 was used for the remaining analyses. The convergence analysis was reinforced with the frequency spectra, and it can be seen that the experimental and numerical results had a stronger correlation.

Tables II and III present the values (f_k) of the active frequencies f_i, $i = 1, \ldots, 5$ and their corresponding amplitude (A_k). These values include the numerical and experimental results obtained for each mesh and time step value. The FFT shows that the numerical simulations can replicate the experimental problem. The active frequencies in both cases include the imposed frequency and its exact multiples. With respect to the FFT results for the CP1 and CP3 signals, the active frequencies are the same, which was not evident in the height-evolution curves. Regarding the amplitude of the frequencies, for all cases, the one with the highest value is the one that matches the frequency imposed, and the amplitudes of its multiples decrease from f_2 to f_5.

In Fig. 5, some instantaneous snapshots obtained using the image-tracking technique are compared with the numerical solutions for the base case with $f = 0.45$ Hz.

Finally, Fig. 6 presents a second comparison between the experimental and numerical results obtained using an imposed frequency of $f = 0.5$ Hz. This figure shows the sensitivity of the problem to changes in the excitation frequency. The results of the simulation are, in general, in good agreement with those of the experiments except for certain cases where the surge of the breaking waves is close [Fig. 6(a)];

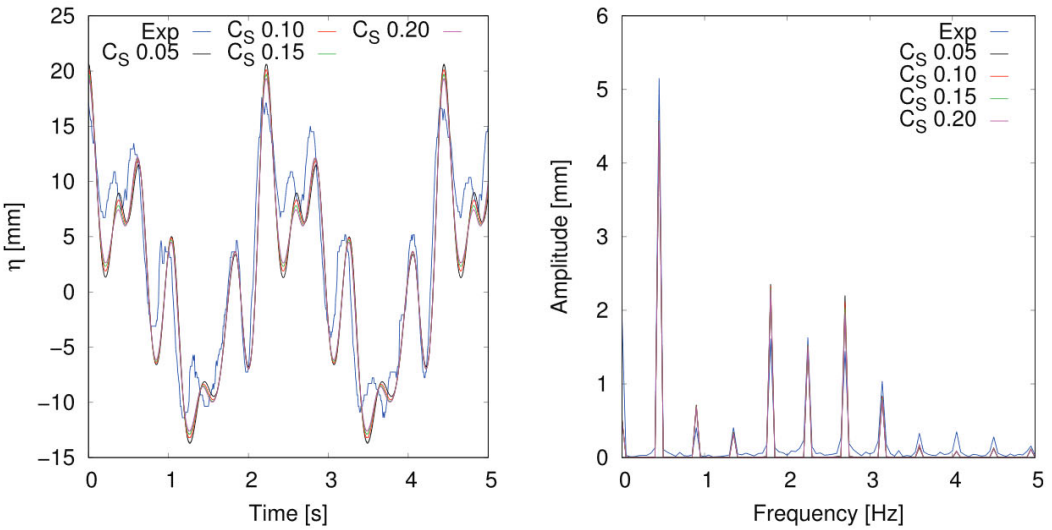

FIG. 8. Influence of the Smagorinsky coefficient (C_S) on wave evolution at CP3 for (a) the steady-state case with $f = 0.45$ Hz and (b) its FFT.

however, the capability of the numerical method to reproduce the real physical behavior of the problem is verified.

B. Effect of the time-integration scheme and the Smagorinsky coefficient

After determining the appropriate mesh and time step (M_2 and δt_2), we performed numerical tests by evaluating the effect of the temporal integrator and the Smagorinsky coefficient on the numerical approximation. The analyzed problem corresponds to the base case, with $f = 0.45$ Hz.

As described in Subsection IV A, convergence in the time analysis was performed using the second-order scheme. The effect of the time marching scheme was evaluated using the first-, second-, and third-order BDF methods. The analysis was performed using a fixed time step value (δt_2). As shown in Fig. 7, the height evolution at CP2 was tracked using the three time-integration schemes. The graph in Fig. 7(a) shows the first 20 s of simulation (from the rest state). Figure 7(b) shows 5 s of simulation of the fully developed flow. Finally,

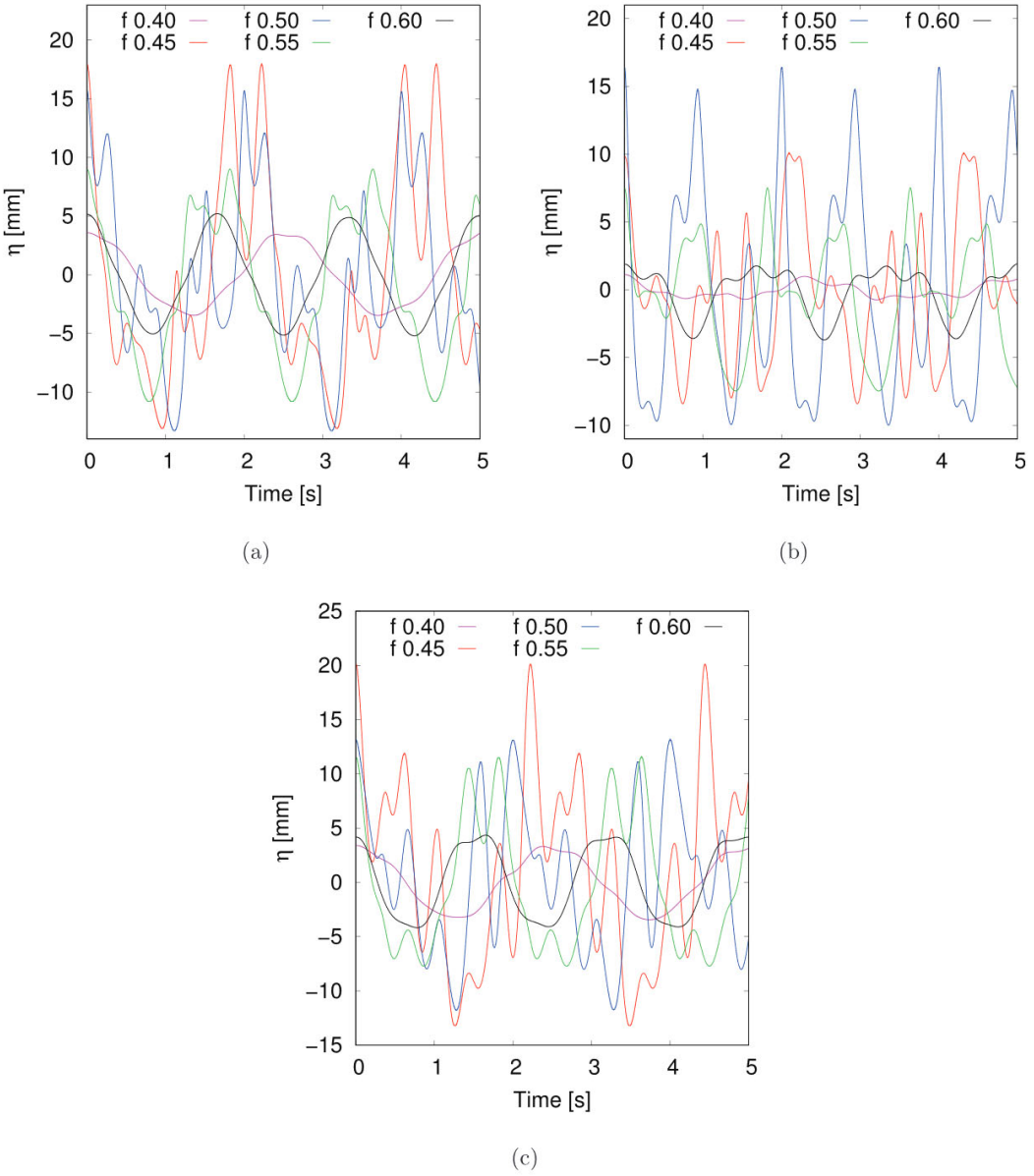

FIG. 9. Effect of imposed frequency (f) on free-surface time-dependent behaviors at (a) CP1, (b) CP2, and (c) CP3.

the graph in Fig. 7(c) shows the active frequencies obtained using each time-integration scheme, including the experimental solution. The exact values of each frequency and its amplitudes are listed in Table IV.

Figure 7 and Table IV show that the order of the time-integration scheme, at least for $\delta t = \delta t_2$, does not influence the result. Regarding the capability of the integration schemes to solve the sloshing problem, all three schemes, including the conditionally stable third-order scheme, could accurately reproduce the problem. With respect to the frequency spectrum, it can be seen that all methods reproduced the same active frequencies, and in particular, BDF2 and BDF3 had practically the same A_k values.

Figure 8 depicts the effect of the Smagorinsky coefficient on the solution of the problem. The coefficient value C_S was varied from 0.05 to 0.2. As in the time integration analysis, the height evolution at CP3 was evaluated. Figure 8(a) shows 5 s of simulation of the fully developed flow. Figure 8(b) shows the active frequencies obtained using each Smagorinsky coefficient, including the experimental solution. The exact values of each active frequency and their amplitudes are listed in Table V. The results show that the solution is practically invariant with changing values of the Smagorinsky coefficient and that the active frequencies obtained from the FFT are practically the same for all cases. From the numerical viewpoint, this result is interesting because in the modeling, the value of the Smagorinsky coefficient can be changed without affecting the solution in terms of the nonlinear convergence of the method. In general, the higher the value of the coefficient, the better the non-linear convergence of the system of equations.

C. Effect of the imposed frequency on free-surface problems

The results presented in Figs. 5 and 6 show the sensitivity of the dynamic behavior of the waves when the frequency is varied from $f = 0.45$ Hz to $f = 0.5$ Hz. In this subsection, the same problem is solved numerically for $f = 0.4$ Hz, $f = 0.45$ Hz, $f = 0.5$ Hz, $f = 0.55$ Hz, and $f = 0.6$ Hz. The height evolution for the three control points is presented in Fig. 9 for each frequency, and the active frequencies obtained through an FFT analysis are presented in Table VI for CP2.

The results presented in Fig. 9 show that the amplitude of the wave is low for $f = 0.4$ Hz and drastically increases for $f = 0.45$ Hz and $f = 0.5$ Hz. However, it decreases for $f = 0.55$ Hz and $f = 0.6$ Hz. As observed through the numerical simulation, the natural frequency of the system should be close to $f = 0.5$ Hz. Table VI shows that for all cases, harmonic frequencies appear. For some cases, for example, $f = 0.5$ Hz, the active frequency with the highest amplitude does not coincide with f.

D. Effect of the step height on free-surface problems

Sloshing is generally analyzed for geometries with constant heights. The inclusion of a step is novel, especially when the experimental and numerical results are included. In this subsection, the effect of the step height is analyzed numerically. The study was conducted in two parts: in the first part, the step height was changed for a fixed level of fluid, measured from the deepest branch (referred to as the H constant), and in the second part, the step height was changed, while the volume of the fluid remained constant (referred to as the v constant).

TABLE VI. Five principal active frequencies in order of amplitude obtained using the FFT of the numerical imposed frequency responses at CP2. f_k is in Hz, and A_k is in mm.

	f 0.40 (Hz)		f 0.45 (Hz)		f 0.50 (Hz)		f 0.55 (Hz)		f 0.60 (Hz)	
	f_k	A_k	f_k	A_k	f_k	A_k	f_k	A_k	f_k	A_k
f_1	0.4	0.32	0.45	1.6	1	3.96	1.1	2.29	1.8	2.35
f_2	0.8	0.14	0.9	1.57	2	2.12	0.55	1.37	0.6	1.11
f_3	…	…	1.8	1.44	3	1.54	2.75	0.53	1.2	0.5
f_4	…	…	2.7	1.32	0.5	1.33	2.2	0.48	2.4	0.12
f_5	…	…	1.35	1.09	1.5	1.26	1.65	0.34	…	…

The numerical study was performed using the base-case frequency of $f = 0.45$ Hz.

In summary, the step heights analyzed for the H constant case (using $H = 100$ mm) are $h_{H,1} = 10$ mm, $h_{H,2} = 20$ mm, $h_{H,3} = 30$ mm, $h_{H,4} = 40$ mm, and $h_{H,5} = 50$ mm. For this analysis, because the fluid height remains constant and the step height varies, the volume of the fluid decreases as the step size increases. In the second analysis, the fluid volume is unchanged and the effect of the step size on the wave dynamics is evaluated. For this case, the constant volume is associated with a step height of $h = 30$ mm and a depth of the right branch of $H = 100$ mm, which results in a volume of $v = 0.006\,8$ m^3. When this value is used and the step height is modified, the fluid

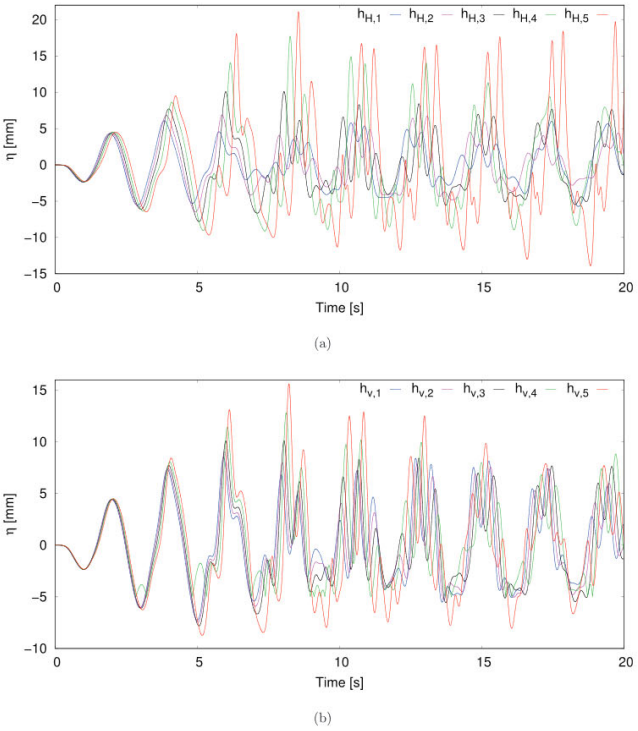

FIG. 10. Effect of the step height in the initial transient regimen at CP1 for the cases of (a) constant H and (b) constant v.

heights must be modified accordingly, which results in five different values: $H_{v,1} = 90$ mm, $H_{v,2} = 95$ mm, $H_{v,3} = 100$ mm, $H_{v,4} = 105$ mm, and $H_{v,5} = 110$ mm, referring to the step heights $h_{v,1} = 10$ mm, $h_{v,2} = 20$ mm, $h_{v,3} = 30$ mm, $h_{v,4} = 40$ mm, and $h_{v,5} = 50$ mm, respectively. With respect to the mesh, a configuration similar to that of mesh M_2 is used for each case.

Regarding the analysis of the step height, Fig. 10(a) shows the initial transients for the cases of constant height and Fig. 10(b) for the cases of constant volume. For the first case, the maximum amplitudes are greater for $h_{H,5}$, whereas for the second case, there are no significant differences in the amplitudes once the flow has developed.

In Fig. 11, the evolution of the fluid height is plotted for CP1 for the two cases analyzed in this subsection. It can be seen that to achieve the flow developed, the numerical approximations require a longer calculation time as the step size decreases; the calculation time increases

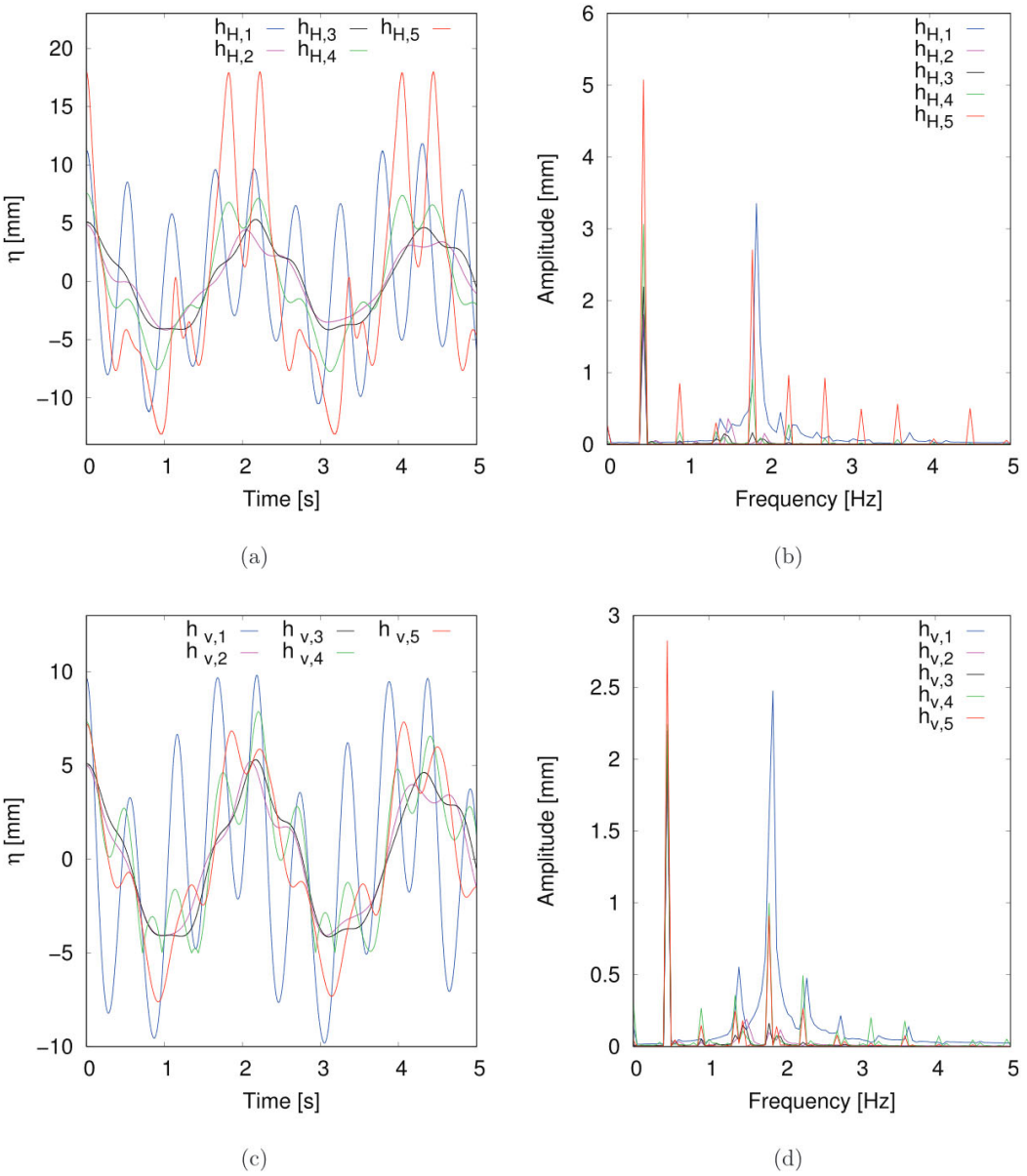

FIG. 11. Effect of the step height (h) in the steady-state time periodic regime at CP1 for [(a) and (b)] constant H and [(c) and (d)] constant v. Free-surface behavior and its FFT (left to right).

from approximately 40 s for both cases with $h = 50$ mm to 420 s for both cases with $h = 10$ mm.

To visualize the effect of the change in the step height in greater detail, for the two cases studied, Fig. 11 shows a time interval in which the problem has already developed in time. In this figure, we can clearly observe a direct relationship between the wave height and the step height when the fluid height is kept constant [Fig. 11 (top)]. In contrast, in the case of constant volume [Fig. 11 (bottom)], the behavior is different: the wave height increases with the decreasing step size. The active frequencies for each case are listed in Tables VII and VIII. Based on this analysis, we observe that the imposed frequency is present in all signals, regardless of the height of the step; nevertheless, different harmonic and sub-harmonic frequencies appear depending on the case analyzed. These trends are practically invariant even if the filling level varies, regardless of whether the total volume of the fluid is unchanged. However, when the total mass of the systems is preserved, it seems to play a damping role mainly for the smaller steps.

E. Effect of viscosity on free-surface problems

It is well-known that sloshing problems are dominated by inertial effects. In this section, the effect of fluid viscosity on the wave dynamics is described. Two numerical tests were performed. For the first one, three Newtonian fluids of different viscosities, water, vegetable oil ($\rho = 912.4$ kg/m^3 and $\mu = 0.071$ Pa s), and SAE 10W-60 engine oil ($\rho = 850.4$ kg/m^3 and $\mu = 0.381$ Pa s), were used. The second test involved the use of non-Newtonian fluids of the power-law type. Specifically, we used carboxymethylcellulose (CMC) diluted with distilled water. For this test, the properties of the fluid were obtained from a previous experimental study,[62] where a rotational viscometer at five temperatures was used. The constitutive parameters were fitted to the experimental data using the power-law model by nonlinear regression analysis. The consistency and power-law indexes used for the numerical tests and the nomenclature used to refer to each fluid are presented in Table IX.

Figure 12 shows that the temporal evolutions of the waves from the rest state to the developed flow are very similar in both the Newtonian [Fig. 12(a)] and non-Newtonian [Fig. 12(b)] cases. This fact confirms that sloshing problems are dominated by inertia, at least in the wave dynamics, and that the fluid viscosity is not a determinant physical parameter.

Finally, Fig. 13, presents the developed flow for each fluid. This figure shows that for the Newtonian fluids [Fig. 13 (top)], a higher

TABLE VII. Five principal active frequencies in order of amplitude obtained using FFT of numerical height step responses in the constant H case at CP1. f_k is in Hz, and A_k is in mm.

	$h_{H,1}$		$h_{H,2}$		$h_{H,3}$		$h_{H,4}$		$h_{H,5}$	
	f_k	A_k	f_k	A_k	f_k	A_k	f_k	A_k	f_k	A_k
f_1	1.85	3.36	0.45	1.81	0.45	2.2	0.45	3.07	0.45	5.81
f_2	0.45	1.66	1.5	0.36	1.8	0.16	1.8	0.92	1.8	2.44
f_3	2.15	0.45	1.95	0.15	1.45	0.15	2.25	0.28	2.25	1.25
f_4	1.4	0.36	…	…	1.35	0.08	1.35	0.18	2.7	0.87
f_5	2.3	0.28	…	…	…	…	0.9	0.19	0.9	0.75

TABLE VIII. Five principal active frequencies in order of amplitude obtained using FFT of numerical height step responses in the constant v case at CP1. f_k is in Hz, and A_k is in mm.

	$h_{v,1}$		$h_{v,2}$		$h_{v,3}$		$h_{v,4}$		$h_{v,5}$	
	f_k	A_k	f_k	A_k	f_k	A_k	f_k	A_k	f_k	A_k
f_1	1.85	2.48	0.45	2.04	0.45	2.2	0.45	2.24	0.45	2.83
f_2	0.45	1.97	1.5	0.19	1.8	0.16	1.8	1	1.8	0.92
f_3	1.4	0.55	1.95	0.12	1.45	0.15	2.25	0.5	2.25	0.26
f_4	2.3	0.48	1.8	0.1	1.35	0.08	1.35	0.36	1.35	0.25
f_5	2.75	0.22	…	…	…	…	0.9	0.27	1.45	0.18

TABLE IX. Properties of different concentrations C of CMC diluted with distilled water using the power-law constitutive model at a temperature of 20° C.

Nomenclature	Concentration (m^3/kg)	Density (kg/m^3)	m (Pa s^n)	n
CMC C10	10	998.2	0.057 4	0.571 6
CMC C20	20	998.2	0.084 8	0.494 5
CMC C30	30	998.2	0.129 3	0.464 9

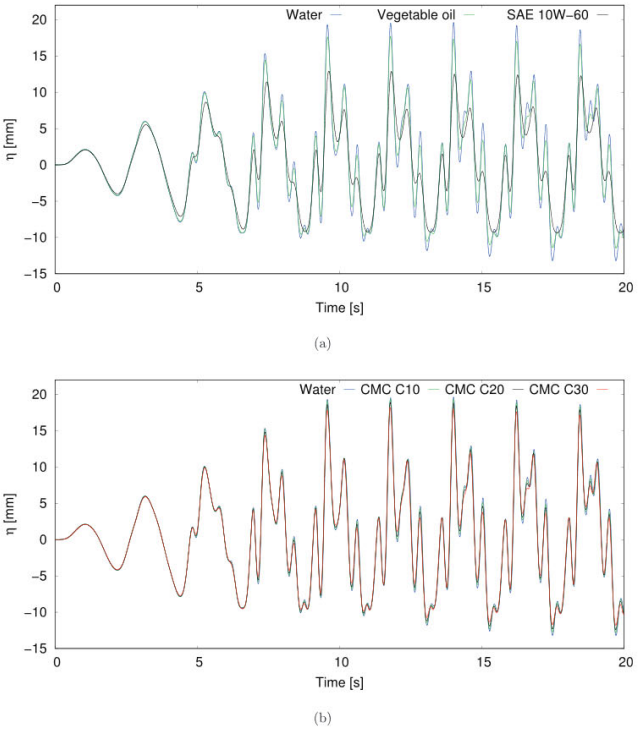

FIG. 12. Effect of rheological properties of fluids in the initial transient regime at CP3 for (a) Newtonian and (b) non-Newtonian cases.

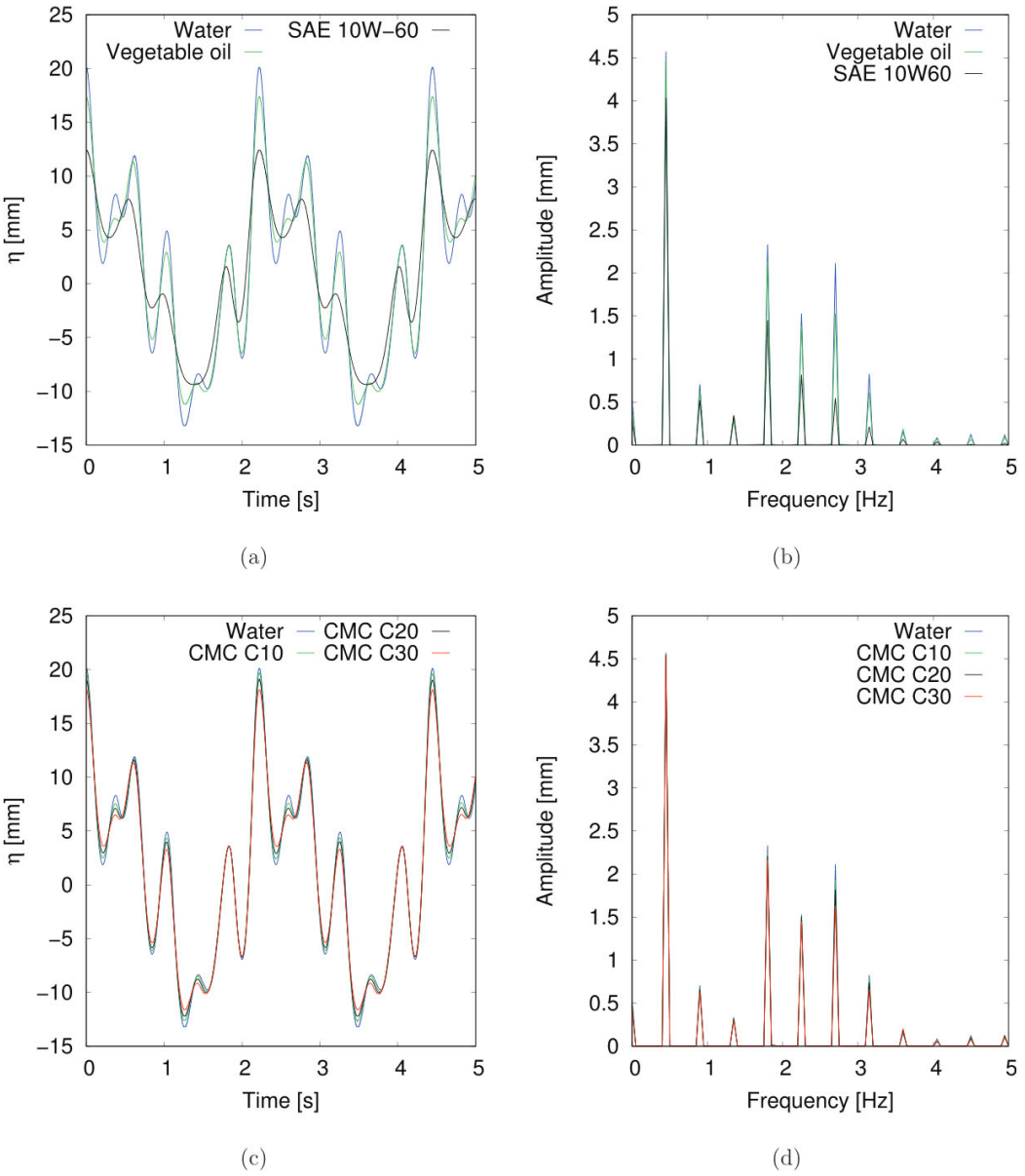

FIG. 13. Effect of rheological properties of fluids in the steady-state time-dependent regime at CP3 for [(a) and (b)] Newtonian fluids and [(c) and (d)] non-Newtonian fluids: time-dependent behavior (left) of the free surface and its FFT (right).

viscosity increases wave damping. For non-Newtonian cases [Fig. 13 (bottom)], even when the fluids had well-defined pseudoplastic behavior, no considerable differences were observed. With respect to the active frequencies listed in Table X, the idea that viscosity is not a determinant parameter is reinforced. Although Fig. 13 shows different behaviors for the free-surface evolution with different fluid models, FFT analysis revealed that the signals practically coincide in time and that only the amplitudes exhibit consistent differences when the fluid properties are varied. These differences can be attributed to differences in viscosity.

V. CONCLUSIONS

In this study, the sloshing in a stepped-based tank was exhaustively analyzed using numerical and experimental techniques. The numerical method was built on a VMS finite element framework, where the free surface was updated using a two-fluid fixed-mesh

TABLE X. Five principal active frequencies in order of amplitude, obtained using FFT of numerical Newtonian and non-Newtonian viscosity responses at CP3. f_k is in Hz, and A_k is in mm.

	Water		Vegetable oil		SAE 10W-60		CMC C10		CMC C20		CMC C30	
	f_k	A_k	f_k	A_k	f_k	A_k	f_k	A_k	f_k	A_k	f_k	A_k
f_1	0.45	4.57	0.45	4.47	0.45	4.03	0.45	4.55	0.45	4.54	0.45	4.53
f_2	1.8	2.33	1.8	2.14	1.8	1.45	1.8	2.24	1.8	2.22	1.8	2.17
f_3	2.7	2.11	2.7	1.53	2.25	0.82	2.7	1.93	2.7	1.82	2.7	1.63
f_4	2.25	1.53	2.25	1.39	2.7	0.55	2.25	1.53	2.25	1.51	2.25	1.45
f_5	3.15	0.83	0.9	0.62	0.9	0.52	3.15	0.79	3.15	0.74	3.15	0.66

method improved with an ALE algorithm, including a remeshing technique. The model was validated using experimental data obtained in this study. In addition, several physical and numerical aspects were evaluated in detail. The main findings can be summarized as follows:

- The layered adaptive-mesh strategy enables the approximation of accurate results for sloshing problems without increasing the number of elements.
- For the analyzed sloshing problems, the use of high orders in time schemes does not improve the numerical results significantly.
- The turbulence model used does not considerably affect the free-surface behavior even if it is needed to improve the nonlinear convergence of the problem.
- The variation of the imposed frequency, e.g., from $f = 0.4$ to $f = 0.45$ Hz, implies that the maximum wave amplitudes increases from 3 mm to 20 mm for CP3, which also happens for CP1 and CP2. This behavior means that a small variation in the imposed frequency motion strongly affects the free-surface evolution in the present experiment.
- The step height has notable effects on flow behavior.
- The viscosity of the fluid, including non-Newtonian effects, does not affect the free-surface predictions on time, as revealed by FFT analyses; however, the wave amplitudes are modified. This could be attributed to the fact that the problem is strongly convective dominant.

ACKNOWLEDGMENTS

The authors thank Ing. José Flores for his collaboration in the experimental work. This study was partially funded by the Chilean Council for Scientific and Technological Research, CONICYT (FONDECYT, Grant Nos. 11160160 and 1170620) and Vice-Presidency of Research, Development and Innovation of the Universidad de Santiago de Chile (VRIDEI-USACH Project No. 052016C) through the program Work Scholarship for Students in Research Work 2020 (Grant Nos. USA2055_IMEC2020 and USA2055_IMEC12020) and for Universidad de Santiago de Chile, USACH, DICYT 022016CDB.

DATA AVAILABILITY

The data that support the findings of this study are available from the corresponding author upon reasonable request.

REFERENCES

[1]S. Hasheminejad and M. Aghabeigi, "Sloshing characteristics in half-full horizontal elliptical tanks with vertical baffles," Appl. Math. Modell. **36**, 57–71 (2012).
[2]F. Viola, F. Gallaire, and B. Dollet, "Sloshing in a Hele–Shaw cell: Experiments and theory," J. Fluid Mech. **831**, R1 (2017).
[3]N. Weber, P. Beckstein, W. Herreman, G. Horstmann, C. Nore, F. Stefani, and T. Weier, "Sloshing instability and electrolyte layer rupture in liquid metal batteries," Phys. Fluids **29**, 054101 (2017).
[4]M. Moslemi, A. Farzin, and M. Kianoush, "Nonlinear sloshing response of liquid-filled rectangular concrete tanks under seismic excitation," Eng. Struct. **188**, 564–577 (2019).
[5]Z. Liu, Y. Feng, G. Lei, and Y. Li, "Fluid sloshing dynamic performance in a liquid hydrogen tank," Int. J. Hydrogen Energy **44**, 13885–13894 (2019).
[6]J. Frandsen, "Sloshing motions in excited tanks," J. Comput. Phys. **196**, 53–87 (2004).
[7]S. Hasheminejad and H. Soleimani, "An analytical solution for free liquid sloshing in a finite-length horizontal cylindrical container filled to an arbitrary depth," Appl. Math. Modell. **48**, 338–352 (2017).
[8]C. Zhang, G. Xiang, B. Wang, X. Hu, and N. Adams, "A weakly compressible SPH method with WENO reconstruction," J. Comput. Phys. **392**, 1–18 (2019).
[9]B. Sanderse and A. Veldman, "Constraint-consistent Runge–Kutta methods for one-dimensional incompressible multiphase flow," J. Comput. Phys. **384**, 170–199 (2019).
[10]O. Faltinsen, O. Rognebakke, I. Lukovsky, and A. Timokha, "Multidimensional modal analysis of nonlinear sloshing in a rectangular tank with finite water depth," J. Fluid Mech. **407**, 201–234 (2000).
[11]M. Cruchaga, R. Reinoso, M. Storti, D. Celentano, and T. Tezduyar, "Finite element computation and experimental validation of sloshing in rectangular tanks," Comput. Mech. **52**, 1301–1312 (2013).
[12]M. Antuono, A. B. C. Lugni, and M. Brocchini, "A shallow-water sloshing model for wave breaking in rectangular tanks," J. Fluid Mech. **746**, 437–465 (2014).
[13]L. Battaglia, M. Cruchaga, M. Storti, J. D'Elía, J. N. Aedo, and R. Reinoso, "Numerical modelling of 3D sloshing experiments in rectangular tanks," Appl. Math. Modell. **59**, 357–378 (2018).
[14]J. N. Aedo, M. Cruchaga, and E. C. del Barrio, "Study on the dependence with the filling level of the sloshing wave pattern in a rectangular tank," Phys. Fluids **32**, 012101 (2020).
[15]O. Faltinsen, O. Rognebakke, and A. Timokha, "Transient and steady-state amplitudes of resonant three-dimensional sloshing in a square base tank with a finite fluid depth," Phys. Fluids **18**, 012103 (2006).
[16]A. Royon-Lebeaud, E. Hopfinger, and A. Cartellier, "Liquid sloshing and wave breaking in circular and square-base cylindrical containers," J. Fluid Mech. **577**, 467–494 (2007).
[17]T. Ikeda, R. Ibrahim, Y. Harata, and T. Kuriyama, "Nonlinear liquid sloshing in a square tank subjected to obliquely horizontal excitation," J. Fluid Mech. **700**, 304–328 (2012).

[18]P. Caron, M. Cruchaga, and A. Larreteguy, "Study of 3D sloshing in a vertical cylindrical tank," Phys. Fluids **30**, 082112 (2018).
[19]E. Castillo, M. Cruchaga, J. Baiges, and J. Flores, "An oil sloshing study: Adaptive fixed-mesh ALE analysis and comparison with experiments," Comput. Mech. **63**, 985–998 (2019).
[20]H. Akyildiz and E. Ünal, "Experimental investigation of pressure distribution on a rectangular tank due to the liquid sloshing," Ocean Eng. **32**, 1503–1516 (2005).
[21]M. Cruchaga, C. Ferrada, N. Márquez, S. Osses, M. Storti, and D. Celentano, "Modeling the sloshing problem in a rectangular tank with submerged incomplete baffles," Int. J. Numer. Methods Heat Fluid Flow **26**, 722 (2016).
[22]E. Zamora, L. Battaglia, M. Storti, M. Cruchaga, and R. Ortega, "Numerical and experimental study of the motion of a sphere in a communicating vessel system subject to sloshing," Phys. Fluids **31**, 087106 (2019).
[23]R. Elahi, M. Passandideh-Fard, and A. Javanshir, "Simulation of liquid sloshing in 2D containers using the volume of fluid method," Ocean Eng. **96**, 226–244 (2015).
[24]M. Nekouei and S. Vanapalli, "Volume-of-fluid simulations in microfluidic T-junction devices: Influence of viscosity ratio on droplet size," Phys. Fluids **29**, 032007 (2017).
[25]F. D. Vita, R. Verzicco, and A. Iafrati, "Breaking of modulated wave groups: Kinematics and energy dissipation processes," J. Fluid Mech. **855**, 267–298 (2018).
[26]W. Bai, X. Liu, and C. Koh, "Numerical study of violent LNG sloshing induced by realistic ship motions using level set method," Ocean Eng. **97**, 100–113 (2015).
[27]H.-Z. Yuan, C. Shu, Y. Wang, and S. Shu, "A simple mass-conserved level set method for simulation of multiphase flows," Phys. Fluids **30**, 040908 (2018).
[28]M. Cruchaga, D. Celentano, and T. Tezduyar, "A moving Lagrangian interface technique for flow computations over fixed meshes," Comput. Methods Appl. Mech. Eng. **191**, 525–543 (2001).
[29]M. Cruchaga, D. Celentano, and T. Tezduyar, "Moving-interface computations with the edge-tracked interface locator technique (ETILT)," Int. J. Numer. Methods Fluids **47**, 451–469 (2005).
[30]A. Huerta and W. Liu, "Viscous flow with large free surface motion," Comput. Methods Appl. Mech. Eng. **69**, 277–324 (1988).
[31]Y. Du, C. Wang, and N. Zhang, "Numerical simulation on coupled ship motions with nonlinear sloshing," Ocean Eng. **178**, 493–500 (2019).
[32]T. Tezduyar, M. Behr, S. Mittal, and J. Liou, "A new strategy for finite element computations involving moving boundaries and interfaces—The deforming-spatial-domain/space-time procedure: II. Computation of free-surface flows, two-liquid flows, and flows with drifting cylinders," Comput. Methods Appl. Mech. Eng. **94**, 353–371 (1992).
[33]T. Tezduyar and S. Sathe, "Modelling of fluid–structure interactions with the space–time finite elements: Solution techniques," Int. J. Numer. Methods Fluids **54**, 855–900 (2007).
[34]M. Cruchaga, L. Battaglia, M. Storti, and J. D'Elía, "Numerical modeling and experimental validation of free surface flow problems," Arch. Comput. Methods Eng. **23**, 139–169 (2016).
[35]J. Baiges and R. Codina, "Variational multiscale error estimators for solid mechanics adaptive simulations: An orthogonal subgrid Scale approach," Comput. Methods Appl. Mech. Eng. **325**, 37–55 (2017).
[36]H. Yuan, Y. Wang, and C. Shu, "An adaptive mesh refinement-multiphase Lattice Boltzmann flux solver for simulation of complex binary fluid flows," Phys. Fluids **29**, 123604 (2017).
[37]H. Yang and J. Peng, "Numerical study of the shear-thinning effect on the interaction between a normal shock wave and a cylindrical liquid column," Phys. Fluids **31**, 043101 (2019).
[38]J. Baiges, R. Codina, I. Castañar, and E. Castillo, "A finite element reduced-order model based on adaptive mesh refinement and artificial neural networks," Int. J. Numer. Methods Eng. **121**, 588–601 (2020).
[39]P. Díez and A. Huerta, "A unified approach to remeshing strategies for finite element h-adaptivity," Comput. Methods Appl. Mech. Eng. **176**, 215–229 (1999).
[40]H. Askes and L. Sluys, "Remeshing strategies for adaptive ALE analysis of strain localisation," Eur. J. Mech., A **19**, 447–467 (2000).
[41]C. Zhang, J. Li, L.-S. Luo, and T. Qian, "Numerical simulation for a rising bubble interacting with a solid wall: Impact, bounce, and thin film dynamics," Phys. Fluids **30**, 112106 (2018).
[42]W. Garhuom, S. Hubrich, L. Radtke, and A. Düster, "A remeshing strategy for large deformations in the finite cell method," Comput. Math. Appl. **80**, 2379 (2020).
[43]R. Codina, G. Houzeaux, H. Coppola-Owen, and J. Baiges, "The fixed-mesh ALE approach for the numerical approximation of flows in moving domains," J. Comput. Phys. **228**, 1591–1611 (2009).
[44]A. Coppola-Owen and R. Codina, "A finite element model for free surface flows on fixed meshes," Int. J. Numer. Methods Fluids **54**, 1151–1171 (2007).
[45]H. Coppola-Owen and R. Codina, "A free surface finite element model for low Froude number mould filling problems on fixed meshes," Int. J. Numer. Methods Fluids **66**, 833–851 (2011).
[46]J. Baiges and R. Codina, "The fixed-mesh ALE approach applied to solid mechanics and fluid-structure interaction problems," Int. J. Numer. Methods Eng. **81**, 1557 (2009).
[47]J. Baiges, R. Codina, and H. Coppola-Owen, "The fixed-mesh ALE approach for the numerical simulation of floating solids," Int. J. Numer. Methods Fluids **67**, 1004–1023 (2011).
[48]J. Baiges and C. Bayona, "Refficientlib: An efficient load-rebalanced adaptive mesh refinement algorithm for high-performance computational physics meshes," SIAM J. Sci. Comput. **39**, C65–C95 (2017).
[49]J. Baiges, R. Codina, A. Pont, and E. Castillo, "An adaptive fixed-mesh ALE method for free surface flows," Comput. Methods Appl. Mech. Eng. **313**, 159–188 (2017).
[50]E. Castillo and R. Codina, "Dynamic term-by-term stabilized finite element formulation using orthogonal subgrid-scales for the incompressible Navier–Stokes problem," Comput. Methods Appl. Mech. Eng. **349**, 701–721 (2019).
[51]A. Aguirre, E. Castillo, M. Cruchaga, R. Codina, and J. Baiges, "Stationary and time-dependent numerical approximation of the lid-driven cavity problem for power-law fluid flows at high Reynolds numbers using a stabilized finite element formulation of the VMS type," J. Non-Newtonian Fluid Mech. **257**, 22–43 (2018).
[52]A. Aguirre, E. Castillo, M. Cruchaga, R. Codina, and J. Baiges, "Pseudoplastic fluid flows for different Prandtl numbers: Steady and time-dependent solutions," Int. J. Therm. Sci. **145**, 106022 (2019).
[53]O. Ruz, E. Castillo, M. Cruchaga, and A. Aguirre, "Numerical study of the effect of blockage ratio on the flow past one and two cylinders in tandem for different power-law fluids," Appl. Math. Modell. **89**, 1640–1662 (2021).
[54]C. Hirt, A. Amsden, and J. Cook, "An arbitrary Lagrangian–Eulerian computing method for all flow speeds," J. Comput. Phys. **135**, 203–216 (1997).
[55]T. Hughes, G. R. Feijóo, L. Mazzei, and J.-B. Quincy, "The variational multiscale method—A paradigm for computational mechanics," Comput. Methods Appl. Mech. Eng. **166**, 3–24 (1998).
[56]R. Codina, "A stabilized finite element method for generalized stationary incompressible flows," Comput. Methods Appl. Mech. Eng. **190**, 2681–2706 (2001).
[57]G. Buscaglia, F. Basombrío, and R. Codina, "Fourier analysis of an equal-order incompressible flow solver stabilized by pressure gradient projection," Int. J. Numer. Methods Fluids **34**, 65–92 (2000).
[58]A. González, E. Castillo, and M. Cruchaga, "Numerical verification of a non-residual orthogonal term-by-term stabilized finite element formulation for incompressible convective flow problems," Comput. Math. Appl. **80**, 1009–1028 (2020).
[59]E. Burman and M. Fernández, "An unfitted Nitsche method for incompressible fluid-structure interaction using overlapping meshes," Comput. Methods Appl. Mech. Eng. **279**, 497–514 (2014).
[60]A. Brooks and T. Hughes, "Streamline upwind/Petrov–Galerkin formulations for convection dominated flows with particular emphasis on the incompressible Navier–Stokes equations," Comput. Methods Appl. Mech. Eng. **32**, 199–259 (1982).
[61]S. D. Costarelli, L. Garelli, M. A. Cruchaga, M. A. Storti, R. Ausensi, and S. R. Idelsohn, "An embedded strategy for the analysis of fluid structure interaction problems," Comput. Methods Appl. Mech. Eng. **300**, 106–128 (2016).
[62]F. Yaşar, H. Toğrul, and N. Arslan, "Flow properties of cellulose and carboxymethyl cellulose from orange peel," J. Food Eng. **81**, 187–199 (2007).